

# **Reservoir characterization using crosswell EM inversion: A feasibility study for the Snorre Field, North Sea**

by

**G. Michael Hoversten<sup>1</sup>**

**G. A. Newman<sup>2</sup>**

**H. F. Morrison<sup>3</sup>**

**E. Gasperikova<sup>3</sup>**

**John-Inge Berg<sup>4</sup>**

**Published: Geophysics Vol 66, No. 4 July-August 2001, p1177-1189**

- 1 Lawrence Berkeley National Laboratory
- 2 Sandia National Laboratories
- 3 University of California at Berkeley
- 4 Saga Petroleum ASA

## **ABSTRACT**

The spatial resolution of a commercially available crosswell electromagnetic (EM) system is demonstrated using models derived from three time steps from a reservoir simulation of the Snorre field in the North Sea. The numerical simulation of the Snorre field water flood shows that crosswell EM field measurements provide high sensitivity to changes in the reservoir over time. This sensitivity is achieved by combining the reservoir geometry derived from surface three-dimensional (3D) seismic interpretation, reservoir conductivities at well locations and constrained EM inversion of the reservoir conductivities.

Inversions of two-dimensional (2D) and 3D numerical models show that the changes in conductivity due to changes in water saturation can be quantitatively mapped as a function of time. The inversions provide smooth estimates of the spatial variation of reservoir conductivity that can discriminate between the level of water saturation at different stages of the water flood. Inversions performed on 2D data show that for the Snorre example between 3 and 5 percent Gaussian random noise (depending on the model) can be added without a significant degradation in the inverse models. Two-dimensional inversions of the full 3D data in the Snorre example can map the vertical average conductivity within the reservoir in the interwell region almost as well as when the model is 2D (constant in strike direction). The effect of 3D structure does not seriously degrade 2D inversion in the Snorre example even between wells that lie in a line parallel to structure.

A series of 2D inversions where various constraints and starting models are used demonstrates the importance of incorporating a priori information in the form of starting models and restricting the inversion domain to the reservoir zone. These tests show that totally unconstrained smooth inversions of the interwell volume provide very limited quantitative information. However, when the reservoir geometry is constrained by seismic data and starting models are provided by linear interpolation of conductivities at well locations, the reservoir vertical average conductivity can be predicted to within a few percent by 2D inversion.

The Snorre Field represents a full-scale reservoir with inter-well spacings that exceed 1 km whereas previous work has demonstrated the applicability of cross well EM in shallow reservoirs with well separations on the order of 100 m. The simulations show that given current transmitter and receiver technology the magnetic fields could be measured in the Snorre field in steel cased wells separated from the transmitter by up to 725m.

## **INTRODUCTION**

An essential problem in petroleum production is the development of an accurate reservoir description. This description is the basis for reservoir simulation that guides the management of the field, including the drilling of new wells and the design of enhanced recovery processes. Ideally, the simulator provides a three-dimensional numerical representation of the properties of the reservoir units and the nature of their boundaries. In practice, the reservoir engineer may only have the unit boundaries, provided by

seismic data, limited log data and inhole pump tests. Even with data from multiple wells and interference tests, the problem of accurately predicting the properties in the interwell volume can limit the effectiveness of a reservoir model.

Geophysics is playing an increasingly important role in mapping the rock properties between wells, and in the assignment of model properties in the interwell volume. This is greatly increasing the effectiveness of in-fill drilling, reservoir production and reservoir stimulation. Major review studies by Lake (1990), Shelton and Cross (1989), and Savitt (1987) all stress the importance of this new role for geophysics. Using geophysics to extrapolate borehole data on porosity, saturation and permeability to the interwell volume, and to monitor changes in these reservoir properties over time, has literally revolutionized reservoir engineering.

Methods for inferring porosity based on seismic velocity are now commonly used for inferring interwell variations. Electrical resistivity and sonic logs are currently among the most used well logging techniques because of their dependence on porosity, saturation, temperature and clay (shale) content. Electric logs are used routinely for assessing saturation, movable oil and indirectly, permeability. The reason for this success is that the pore fluid controls the bulk resistivity of most permeable rocks, since the current is carried only by ions in solution. Thus the fractional volume of pore fluid, porosity ( $\phi$ ), pore water resistivity ( $R_p$ ), water saturation ( $S_w$ ) and temperature all control the bulk resistivity of the rock,  $R_b$ . Traditional well logging estimates the resistivity within a few meters (at most) of the borehole. The crosswell electromagnetic technique described here is designed to map the resistivity, or its inverse conductivity, between wells, at interwell distances up to 1km.

The basic theory for the use of low-frequency (where displacement currents can be neglected) EM methods for determining  $R_b$  between wells on a scale useful for reservoir characterization has been detailed in recent papers and theses. These include Zhou (1989), Spies (1992), Zhou et al. (1993), Alumbaugh et al. (1993), Alumbaugh and Morrison (1993, 1995), Spies and Habashy (1995), and Wilt et al. (1995). The analyses in general deal with frequencies above 1 kHz and where the holes are not cased with steel. In contrast to these studies, we consider well separations for a full-scale reservoir at a frequency of 50 Hz.

Although we do not include the additional attenuation and phase shifts of steel cased holes in our analysis we do demonstrate that the attenuation caused by steel cased wells does not preclude measurement of the magnetic fields in the Snorre example.

### **THE SNORRE FIELD**

The Snorre reservoir is located on the Tampen Spur in the Norwegian sector of the Northern North Sea, in approximately 300 meters of water at depths between 2000 to 2700 meters below sea level. The field was discovered in 1979 and production commenced in August 1992. There are two main reservoirs, the Triassic Lunde Formation and the Triassic-Jurassic Statfjord Formation. Each of these reservoirs consists of a network of fluvial sand bodies in a mudstone matrix, deposited in an alluvial setting.

As of 1996 there were 20 wells drilled in this field. Two-thirds of these wells produce oil and gas with the remaining used for water injection. A detailed description of the reservoir characterization of Snorre can be found in Diesen et al. (1995).

Saga Petroleum provided a reservoir simulation of a portion of the field. The simulation covered the area around four existing wells, shown in Figures 1 and 2.

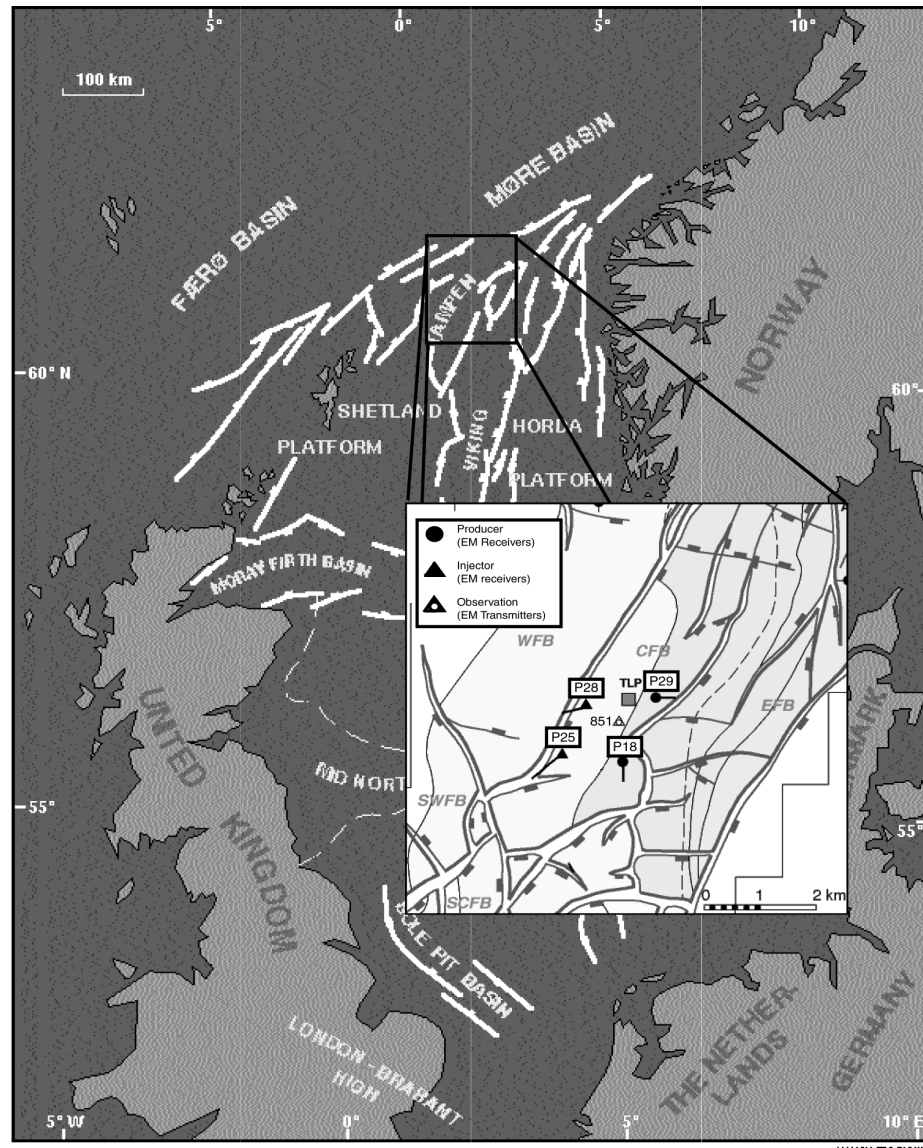


**Figure 1:** Location map for Snorre Field with inset structure map of portion of the Snorre field covered by reservoir simulation. Wells P25 and P28 are water injectors. Wells P18 and P29 are producers. Well 851 is a proposed observation well. The numerical simulation of the cross-well EM experiment used well 851 as the transmitter well and the P18, P25, P28 and P29 receiver wells.

Wells P28 and P25 are down dip water injectors while wells P29 and P18 are up dip producers. Figure 2 shows the depth to the top of the reservoir interval, the Statfjord S1 formation. The total reservoir interval averages 60m in thickness. The cross well EM simulations were designed to use well 851, to be drilled as a fiberglass cased observation

well, for the EM transmitters with wells P18, P25, P28 and P29 used as EM receiver wells. The cross section between 851 and P28 is essentially perpendicular to strike and is used in a 2D example. The remaining cross sections between 851 and wells P18, P25 and P29 cross the structure at various angles with the 851 to P29 cross section running essentially parallel to strike. All 4 well pairs are interpreted using 2D inversion of the 3D numerical model magnetic field responses.

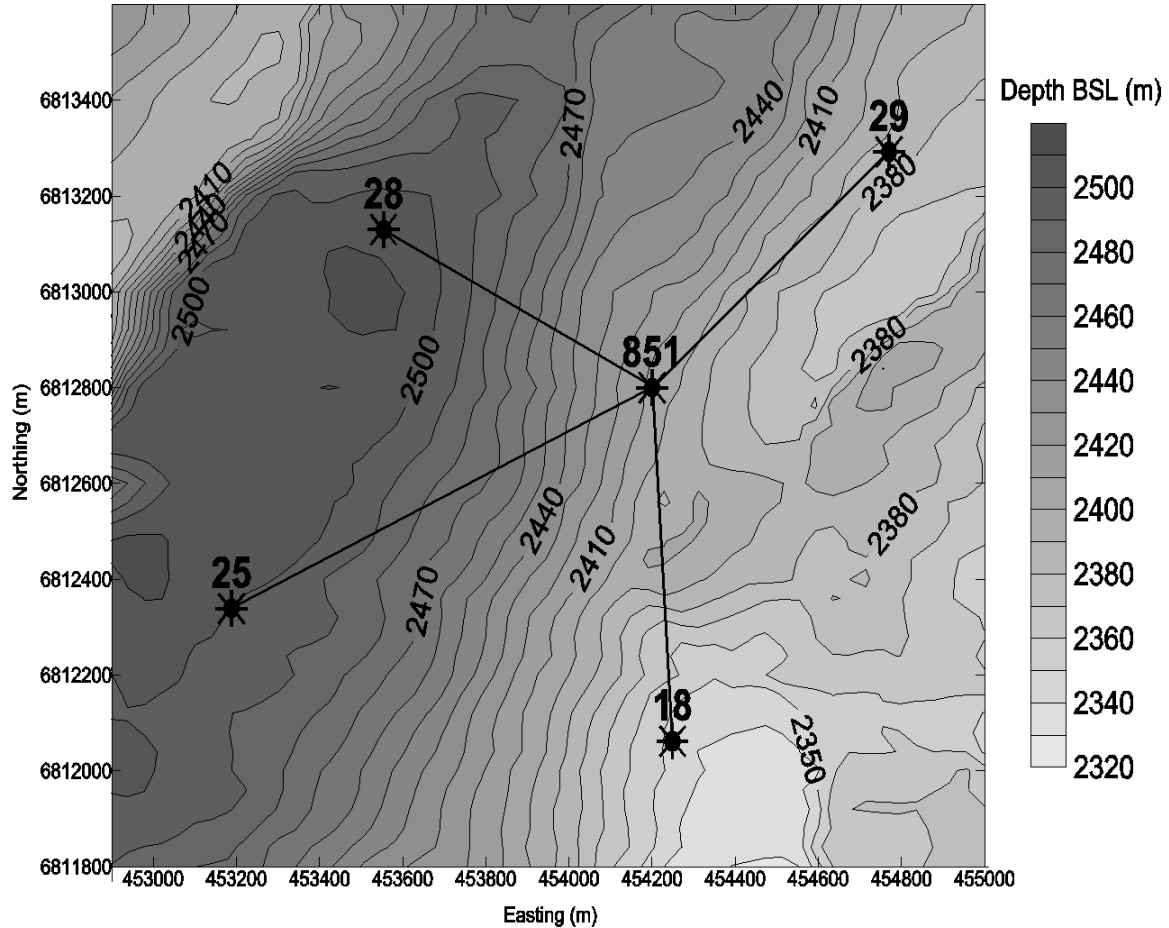


**Figure 2:** Depth below sea level of the top of the reservoir interval. The four crosswell sections considered in the study are shown as black lines between observation well 851 and P25, P28 (water injectors) and P18, P29 (producers).

The reservoir simulation was done using the GeoQuest Eclipse Simulator. Three time snapshots of the reservoir were analyzed. The first time ( $t_0$ ) represented initial conditions at the beginning of production in August 1992. The second time ( $t_{140}$ ) represents July 1, 1997 and the third time ( $t_{160}$ ) represents January 1, 2000. The water saturation values at these three times along with the 3-D seismic top and base of the reservoir were used with a relationship between water saturation and bulk resistivity derived from log data to produce three 3D resistivity models of the reservoir zone.

#### DEPENDENCE OF ELECTRICAL RESISTIVITY ON WATER SATURATION

Figure 3 shows the bulk electrical resistivity ( $R_b$ ) vs.  $S_w$  for samples within the reservoir units from wells P18, P28 and P29 at initial conditions. There is a strong

correlation between  $R_b$  and  $S_w$ , the observed data are fit by a linear log-log relation given by Equation 1, with a  $\chi^2$  of 0.89.

$$R_b = 1.38 * S_w^{-1.7} \quad (1)$$

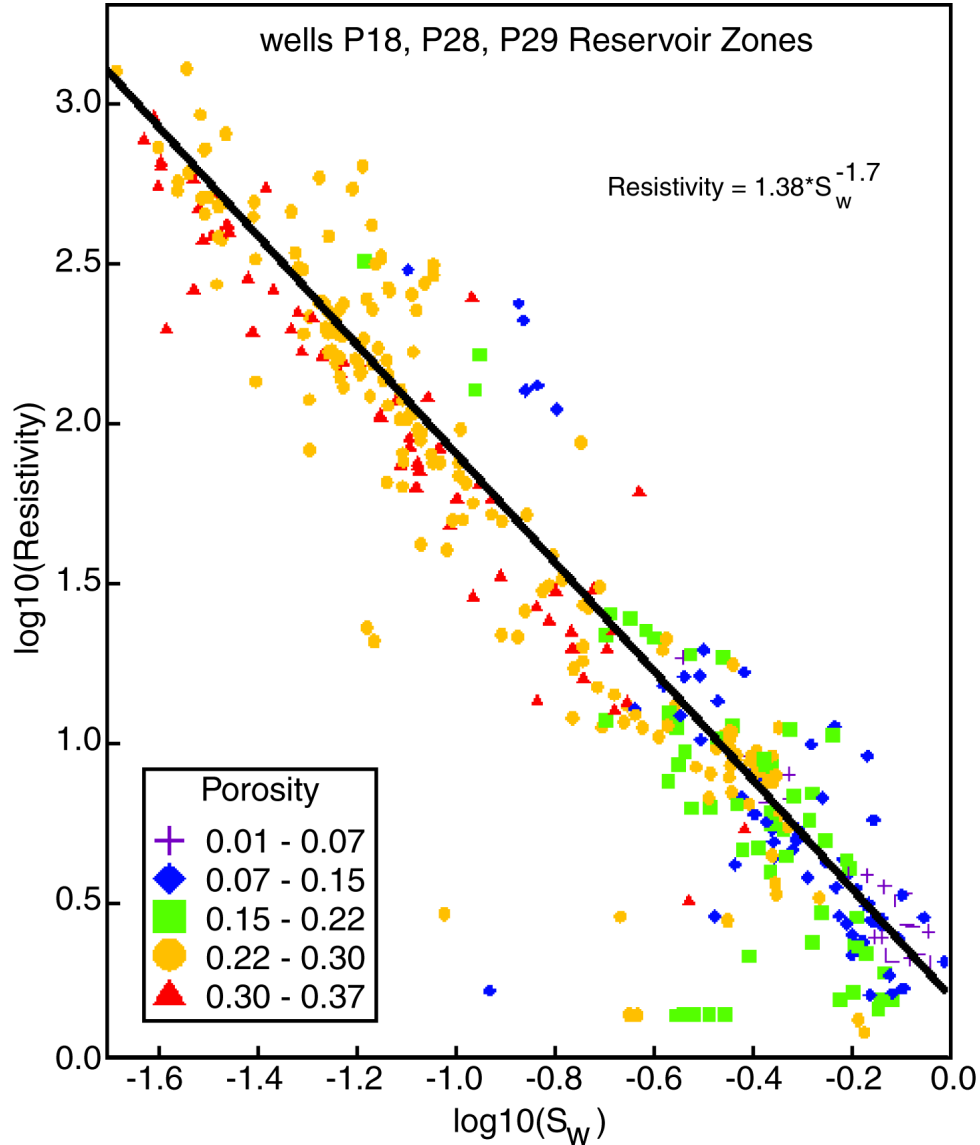


**Figure 3:** Resistivity vs. water saturation for log samples within the reservoir units from wells P18, P28 and P29. The linear log-log regression fit has a Chi squared  $\chi^2 = 0.89$ .

This relation is independent of porosity because reduced porosity at Snorre is caused by clay filling the pore space. The increased conductivity of the clay offsets the decrease in resistivity caused by the reduction in pore space.

If the reservoir resistivity can be mapped between wells there exists the potential of using this relationship for characterizing the reservoir  $S_w$ , and in monitoring changes in  $S_w$  over time as production occurs or as an enhanced recovery process is employed.

Ideally seismic velocity and/or acoustic impedance and resistivity would be mapped as is done in well logging. Velocity and/or acoustic impedance would then be used to map porosity which, combined with known pore water resistivities (from the borehole sampling), would then be used to determine  $S_w$  from the EM data. It is important to stress however that in a given field, with known properties at boreholes, the electrical resistivity itself can be used to extrapolate properties between wells even if the process is empirical for that field.

It must be noted that (1) is strictly only valid at initial conditions within the reservoir. Relationships between  $R_b$  and  $S_w$  will depend on whether the reservoir is water-wet or oil-wet. In particular, Suman & Knight (1997) have studied the behavior of Archie's Law (Archie, 1942) as a function of the rock wettability. They conclude that "Archie's law may be realized only in strongly water-wet systems in which a sufficiently thick water film is present". In addition they note that wettability has a dominant influence on the relationship between water saturation and bulk resistivity of partially saturated rocks and that oil-wet systems display substantially higher saturation exponent values and significant hysteresis between drainage and imbibition cycles. Further, the saturation exponent itself can be a function of saturation. This means that additional laboratory work may be required to derive relationships between  $R_b$  and  $S_w$  that are applicable as water flood proceeds in certain reservoirs due to the nonlinear relationship between resistivity and saturation changes.

Since we lack the necessary laboratory measurements to improve on Equation (1), and since Snorre is a strongly water-wet reservoir, Equation (1) should be a good approximation to the true  $R_b$ - $S_w$  relationship as water flood proceeds. Equation (1) will be used to convert between  $R_b$  and  $S_w$  throughout this work. No pore fluid resistivity term is included in Equation (1) since the pore fluid resistivity,  $R_f$ , is only a few percent different from the resistivity of the injected seawater at reservoir temperatures. Thus, accounting for the mixing of two different resistivity fluids in the pore volume is not required.

### **NUMERICAL EM MODEL PARAMETERS**

We simulate 3D EM fields by solving Maxwell's differential equations with a staggered-grid finite-difference scheme described by Newman (1995). Here the fields are solved on a grid in the frequency domain for vertical magnetic dipole sources in this application.

In this study, models were run using a background resistivity of 2  $\Omega$ -m, representing shale surrounding the reservoir. Vertical magnetic dipole transmitters were simulated in well 851 with receiver locations in the four production wells. Transmitters and receivers were located at 10m intervals from 2320 to 2600 m. Horizontal (radial away from the transmitter) and vertical magnetic fields were calculated at the receiver locations. In these simulations we have ignored the effect of steel casing in the wells on the measurements. We will discuss the casing problem later in the paper.

The transmitter frequency was chosen to be as high as possible subject to the constraint that the farthest source-receiver separations should not be more than 10 skin-depths in the background material. The skin-depth is the distance at which the field strength falls off by a factor of  $1/e$ . The skin-depth ( $\delta$ ), in meters, as a function of resistivity ( $\rho$ ) and frequency ( $f$ ) is approximately given by;

$$\delta \cong 503 * \sqrt{\frac{\rho}{f}} \quad (2)$$

The largest source-receiver separations exist between wells 851 and P25. This distance is approximately  $10 * \delta$  at 50 hertz in the 2  $\Omega$ -m background.

The 10 skin-depth limit was placed on transmitter-receiver separations based on numerical tests of the finite-difference algorithm comparing results to more numerically stable layered-model algorithms. We found that for homogeneous halfspace models when the transmitter-receiver separations became greater than ten skin-depths the 3D results began to differ by more than five percent from the correct layered earth solutions. The resulting limit of ten skin-depths in the numerical models fortunately corresponds with the maximum source-receiver separations achievable in field data measurements observed by Wilt, (Personal Communications).

The choice of mesh parameters such as cell size and overall size of the mesh are critical for accurate numerical EM modeling. For general inhomogeneous 3D models such as the Snorre reservoir, the only way to insure an accurate solution is to first design a mesh that produces solutions that can be checked against accurate 1D codes. Halfspace checks were performed with transmitters located at the top, middle and bottom of well 851 to all four receiver wells. The maximum difference between 1D and 3D solutions was five percent, with an average difference of two percent.

Once a 3D mesh is designed to accurately compute 1D fields, then the 3D structure is added and the solutions are compared as the mesh in the region of the 3D structure is made finer. This is often referred to as a “convergence check”. Once a stable 3D solution is reached that does not change as the mesh is made finer it is deemed correct.

The finite difference cell sizes in the reservoir zone were 40 by 40 by 10 m in the x, y and z directions respectively. Outside of the reservoir zone the cell dimensions were increased to a maximum size of 80 by 80 by 20 until the mesh boundaries were at least two skin depths away from any well in the horizontal directions and four skin depths away from any transmitter or receiver in the vertical direction. Total mesh dimensions were 57 by 50 by 73 in the x, y and z directions respectively. Models required 285 minutes to run on a 500MHz DEC Alpha 21264 processor.

### **PRACTICAL CONSIDERATIONS**

For the results to have immediate practical value it is desirable to consider fields which are large enough to be measured in the field with existing equipment. The Snorre example represents well separations that range between what is currently possible (7 skin depth separation between well 851 and P28) to well separations which are just beyond the



reach of current technology (10 skin depth separations between well 851 and P25). Our 2D study will focus on the cross section between well 851 and well P28. Our 3D study will consider all four well pairs with well 851. Although the 851 to P25 separation (1.1 km) is not feasible with existing equipment, next generation transmitters with increased dipole moment will make this possible. Figure 4 shows the vertical and horizontal components of the magnetic field in well P28 for a transmitter above the reservoir in well 851 at initial conditions. This represents a well separation of 725m.

Existing down-hole receivers have a noise level amplitude of approximately  $4.0 \times 10^{-9} (\text{amp/m}) / \sqrt{\text{Hz}}$  at 50 Hz. Assuming 20 seconds of averaging yields a noise amplitude of,  $\sqrt{(4.0 \times 10^{-9})^2 (\text{amp/m})^2 / \text{Hz} * (1/20)(\text{Hz})} = 8.94 \times 10^{-10} (\text{amp/m})$ .

The vertical magnetic field inside a steel casing embedded in a 2  $\Omega\text{-m}$  whole space for a transmitter-receiver separation of 725 m was calculated using a code developed by Song & Lee (1998). The casing parameters were; outer diameter = 7.5 inch, inner diameter = 6.87 inch, conductivity =  $3.6 \times 10^{+6} \text{ S/m}$  and magnetic permeability = 50 time that of free space. This shows an attenuation of the vertical magnetic field of 0.827 due to a single casing at 50 Hz.

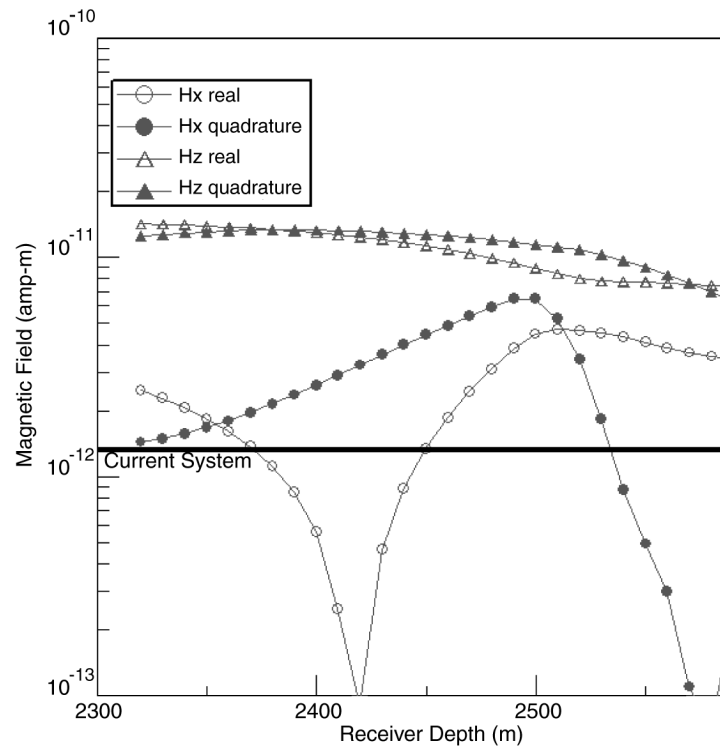


**Figure 4:** Vertical (Hz) and radial (Hx) magnetic field components as a function of receiver depth in well P18 for a vertical magnetic dipole transmitter of unit moment at a depth of 2320m in well 851.

The maximum dipole moment of existing down-hole vertical magnetic dipole transmitters is 1000 amp-turn-meters. Accounting for a transmitter moment of 1000, and an attenuation factor of  $(0.827)^2$  for two casings gives a scaling factor of 684 for the

magnetic fields calculated using a unit dipole moment. Thus for fields for a unit dipole transmitter moment we can scale the noise amplitude down by 684, yielding a coil noise level of  $1.3 \times 10^{-12}$  (amp-m) per unit transmitter moment, which is shown as "Current System" on Figure 4.

Since the noise level is inversely proportional to the square root of the bandwidth (the inverse of the averaging period) increasing the averaging time by a factor of 100 will drop the noise level by a factor of 10, assuming a Gaussian noise distribution.

We have performed inversions using either the vertical magnetic field only or using both horizontal (radial from the transmitter) and vertical magnetic fields to demonstrate the differences. However, the horizontal magnetic field sensors in current equipment are approximately 10 times less sensitive than vertical field sensors due to the geometry constraints of operating in the borehole. Thus, with current equipment, the vertical magnetic field would be preferred in the Snorre application since to acquire horizontal fields would require additional averaging time. Future systems will be capable of larger dipole moments in the transmitters and more sensitive receivers making the measurement of horizontal components at the separations present in the Snorre example feasible.

The effect of steel casing is more difficult than the simple attenuation calculation mentioned above would indicate. In addition to the attenuation, there are large phase shifts introduced which make it essential that some way of estimating the casing response at each source and/or receiver location be available. One approach is the inclusion of a small monitor array in both the transmitter and receiver tools (Lee & Kim 1998). Algorithms for estimating the casing properties have been presented by Wu & Habashy (1994) and Lee & Kim (1998). This subject is beyond the scope of this paper. Becker et al. (1998) and downhole EM equipment manufactures are currently working on systems and data processing techniques for removing the casing response from data prior to inversion.

## **SENSITIVITY OF VERTICAL MAGNETIC FIELD TO CHANGES IN $S_w$**

Before considering the quantitative inversion of the crosswell data it is instructive to look at the changes of the vertical magnetic field as  $S_w$ , and thus  $R_b$ , changes. Figures 5 and 6 show the percent changes in the real (in-phase) and quadrature (out-of-phase) components respectively of the vertical magnetic fields from  $t_0$  to  $t_{140}$  (upper panel) and  $t_{140}$  to  $t_{160}$  (lower panel). The percent changes are defined as  $((t_{140}-t_0)/t_0)*100$ . The real component at  $t_0$  has a zero crossing which causes this calculation to become extremely large at certain points. We have therefore removed any value outside the range  $\pm 500$  percent. This causes the large white area around the central low (panel a, Figure 5). The resistivities of the reservoir zone are shown at the three time steps on the left side of Figure 7.

The largest change is seen in the real component as the reservoir goes from being predominately oil filled with an average  $S_w$  near one percent to an average  $S_w$  near ten

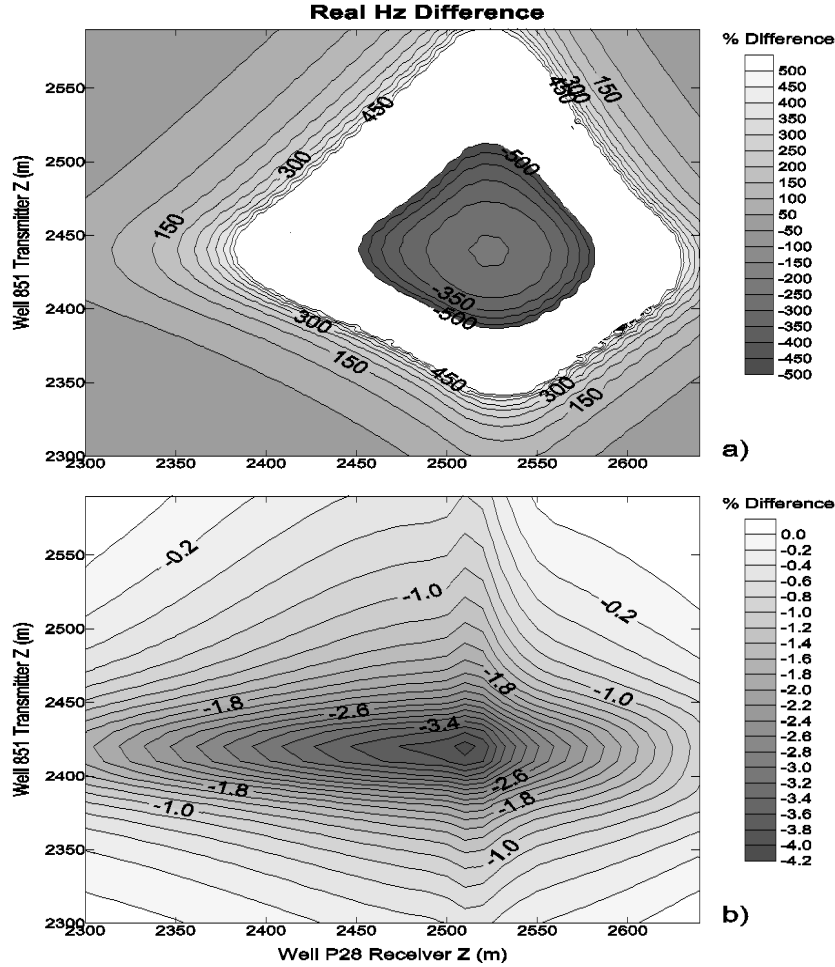


**Figure5:** Percent change in real component of vertical magnetic field. Top panel: change between  $t_0$  and  $t_{140}$ . Bottom Panel: change between  $t_{140}$  and  $t_{160}$ .

percent. A change of over 500% in the real component is seen when the transmitter and receiver are both located in the reservoir zone. The large value of 500% is partially an artifact of the choice of denominator in the percentage calculation since real Hz at  $t_0$  is going through a minimum as the receivers pass through the reservoir. If the fields at  $t_{140}$  are used as the denominator then the change drops to around 85%. The quadrature changes have no minima and are on the order of 30 to 60 % for either choice of denominator in the percent change calculation.

Between time  $t_{140}$  and  $t_{160}$  the average  $S_w$  does not change much but oil is redistributed causing a decrease of  $S_w$  near the 851 (transmitter) well and an increase in  $S_w$  near the P-28 (receiver) well. The conductivity increased between 10 and 20 percent in the bottom portions of the reservoir near the receivers and decreased by as much as 100% in the upper portions of the reservoir near the transmitters. This redistribution of conductivity in the reservoir is reflected in the changes shown in Figure 6. The absolute value of the changes are greatly reduced compared to the changes between  $t_0$  and  $t_{140}$ , with maximum changes of 4 and 10 percent in the real and quadrature components respectively. Although the changes are smaller, reflecting the smaller changes in

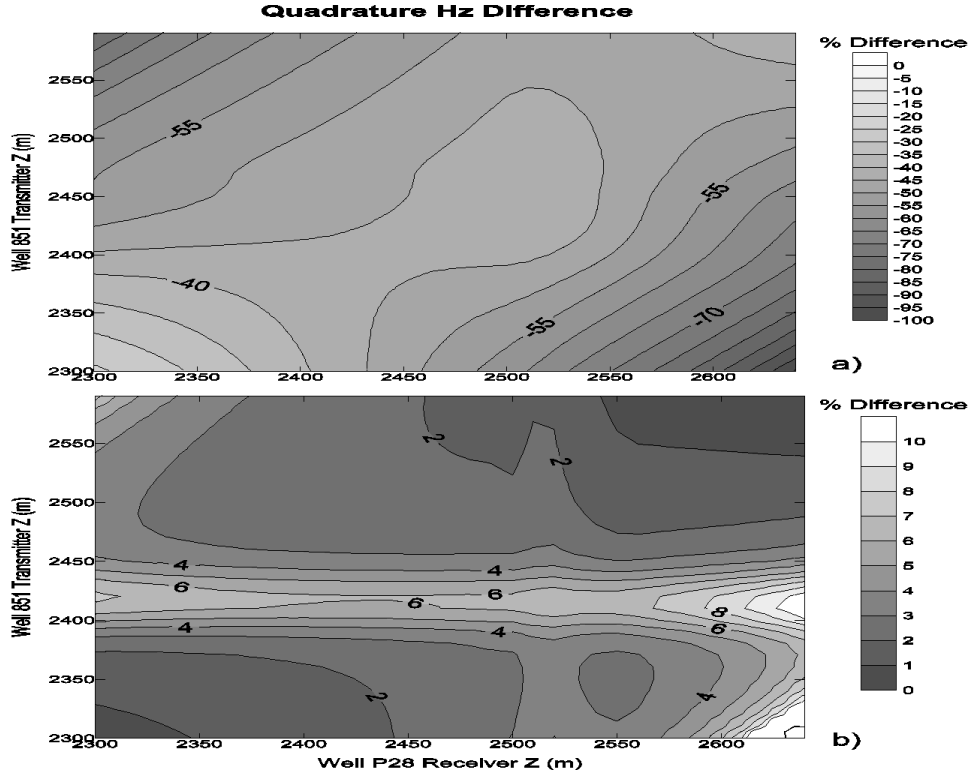


**Figure 6:** Percent changes in quadrature (out-of-phase) component of vertical magnetic field. Top panel: change between  $t_0$  to  $t_{140}$ , Bottom panel: change between  $t_{140}$  to  $t_{160}$ .

reservoir conductivity, the spatial variations are more distinctive, particularly in the quadrature component.

### INVERSION OF 2D DATA

Because it is difficult to separate the inherent limitations of 2D EM inversion from dimensional effects when using a 2D inversion on 3D data, a set of 2D numerical models were generated to represent the cross-section between the P-28 and 851 wells. We refer to 2D as the case where the source is 3D and the structure is 2D, sometimes referred to as 2.5D. Crosswell EM measurements of the real and quadrature vertical magnetic field can routinely be made with standard deviations of one percent or better at well separations of six skin depths in uncased boreholes, (Wilt Personal Communication). It is also observed that the noise level is usually proportional to the total magnetic field. We have assumed an optimistic one percent noise level, thus Gaussian random noise with a standard deviation of one percent of the total magnetic field value was added to numerical model data before inversion. In a later section we demonstrate that up to three percent Gaussian random noise does not significantly degrade the  $t_{140}$  inversion between wells 851 and P28.

We have used a modified version of the inversion algorithm, Appendix A, described by Newman (1995). The algorithm uses the starting model as a reference model ( $\sigma_0$ ) and solves for perturbation about this reference model. Thus the inverse parameters are  $(\sigma - \sigma_0)$ . The regularization smoothing is applied to the perturbation,

$(\sigma - \sigma_0)$ , rather than to  $\sigma$  itself. The reference model was constructed using 3D seismic interpreted top and base reservoir surfaces. The reservoir zone conductivity was defined at the wells from the logs and linearly interpolated between the wells. The reference model had the log values extended without extrapolation to either side away from the wells. The spatial smoothing of the conductivity perturbations was stopped at the reservoir boundaries allowing a sharp jump in conductivity at these boundaries and only cells within the reservoir were free to change in the inversion.

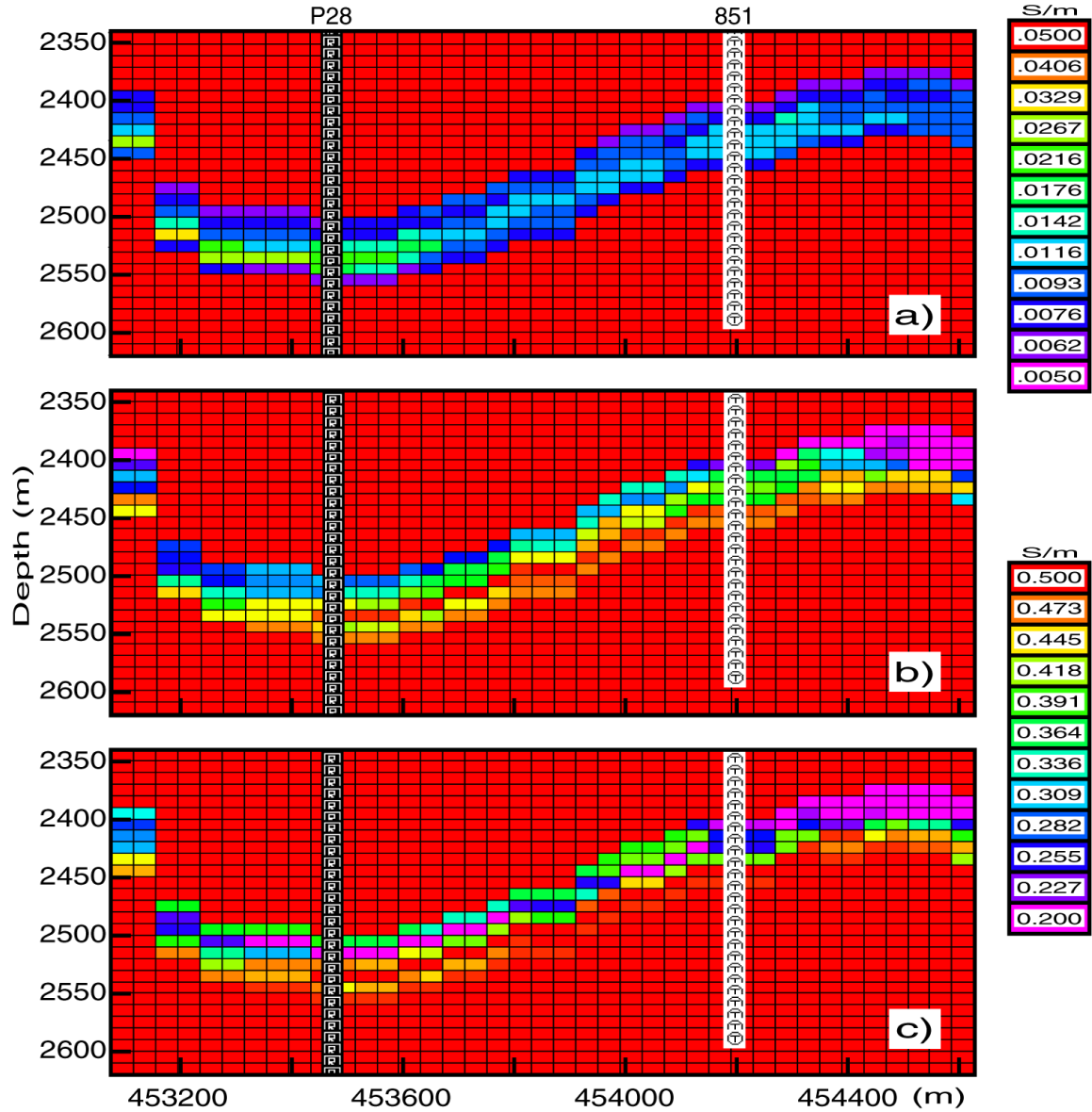


**Figure 7:** Reservoir simulations at times  $t_0$ ,  $t_{140}$  and  $t_{160}$  converted to conductivity using log derived Equation 1.

Figure 7 shows the conductivity cross-sections between the P28 injector (left side) and observation well 851 (right side) at the three time steps ( $t_0$ ,  $t_{140}$ , and  $t_{160}$ ) generated from the reservoir simulation  $S_w$  using Equation (1). The injector well was used for the EM receivers and the observation well was used for the vertical magnetic dipole

transmitters. Figure 8 shows the inverse model sections at the 3 reservoir simulation time steps for comparison with the true conductivity sections shown in Figure 7. Only the vertical magnetic field data was used for the inversions shown in Figure 8. All inversions discussed were terminated when the RMS data misfit fell below 1. Thus all data were fit to within the assumed standard errors.

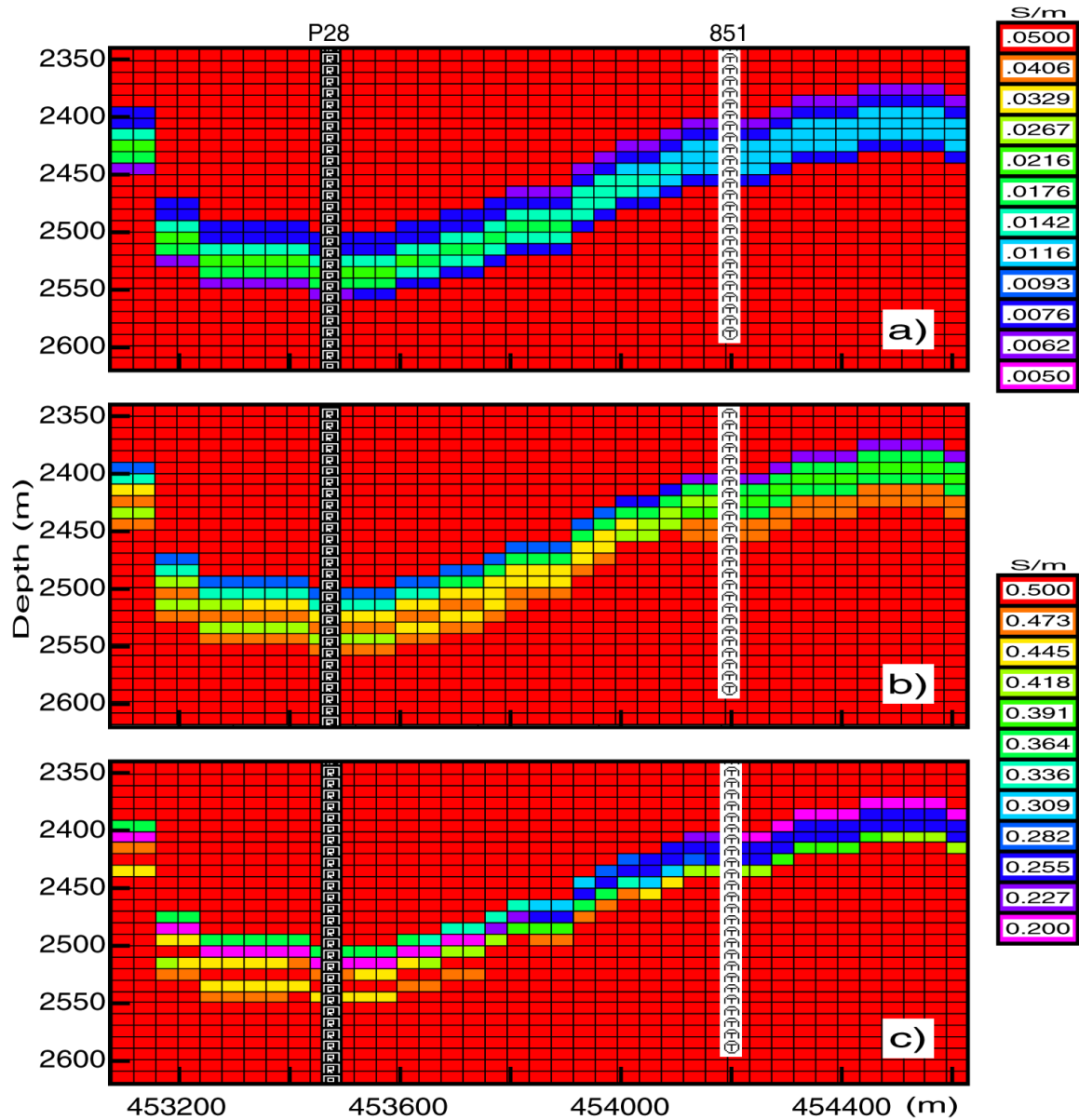


**Figure 8:** Cross-well EM inversions of the numerical data generated from the models shown in Figure 7. The oil build up is shown in the inversion at  $t_{160}$ . The starting model for the reservoir was a linear interpolation of the conductivities at the wells. Water saturation (conductivity) at  $t_0$  is significantly lower than at later times, requiring a change in color tables between  $t_0$  and  $t_{140}$ . Inversion for  $t_{140}$  and  $t_{160}$  are displayed on the same color scale.

At initial conditions,  $t_0$ , when the reservoir is mainly filled with oil and its conductivity is roughly 50 times less than that of the surrounding shale. In these conditions the radial magnetic field strength at the receivers in the vicinity of the

reservoir (these are the data most sensitive to resolving the reservoir conductivity) is twice that of the vertical magnetic field. At the two later times ( $t_{140}$ ,  $t_{160}$ ) the average reservoir conductivity is close to that of the surroundings and the radial magnetic field is nearly an order of magnitude less than the vertical magnetic field. Since the data errors are assumed to be proportional to the total magnetic field, the signal to noise ratio of the vertical magnetic field is significantly lower at  $t_0$  than at  $t_{140}$  or  $t_{160}$ . The reference model constructed from a linear interpolation between the wells of the log conductivities fit the numerical vertical magnetic field data with 1% total field noise to within an RMS of 1, thus the model in panel a) of Figure 8 is the starting model. As will be discussed below, when both the vertical and horizontal fields are used the inversion can improve on the starting model and more accurately map the interwell conductivity at initial conditions.

### PREDICTED WATER SATURATION

In order to see how the crosswell EM models might provide water saturation estimates to improve reservoir simulations the inversions in Figure 8 were converted to water saturation using Equation (1). Because the reservoir is thin relative to its lateral extent a useful parameter to summarize its properties is the vertical average conductivity. Profiles between wells P28 and 851 of the true and predicted vertical average conductivity and water saturation within the reservoir are plotted in Figure 9 for the three

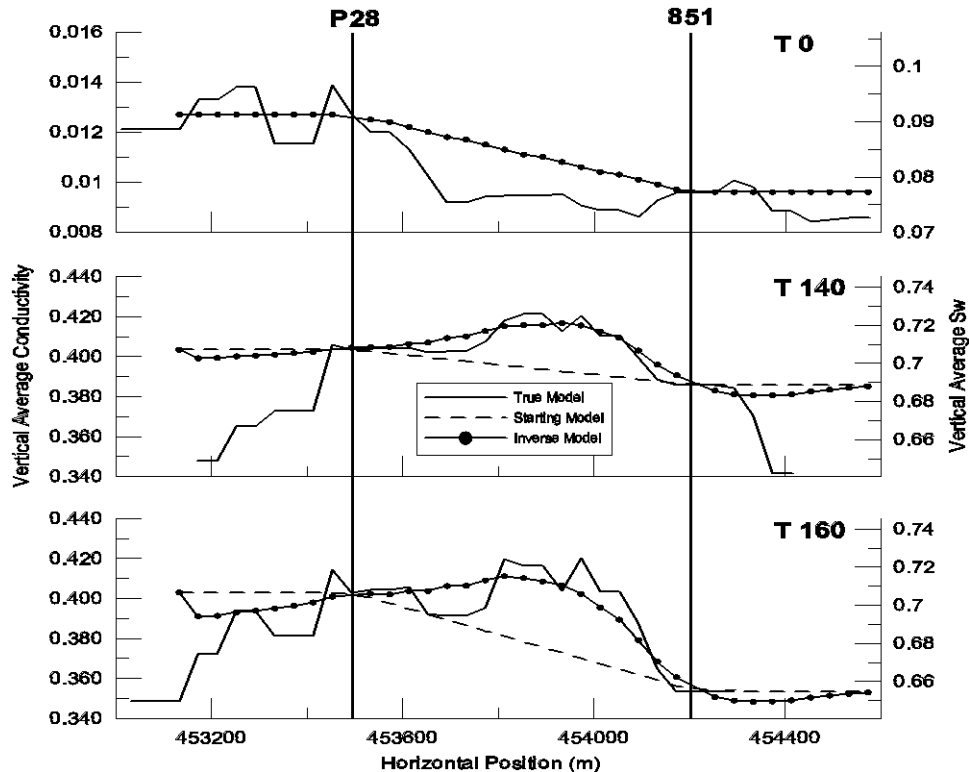


**Figure 9:** Comparison of vertically averaged conductivity and water saturation within the reservoir and that estimated from the cross-well inversions of numerical vertical magnetic field data. Well P28 is located at 453474 m; well 851 is located at 454200 m. Initial conditions are shown in the top panel. The middle panel shows reservoir at  $t_{140}$ . The bottom panel shows the reservoir at  $t_{160}$ .

time steps of the simulation. There is a change in the scale between  $t_0$  and  $t_{140}$ . The inversions provide laterally smoothed versions of the true vertical averages.

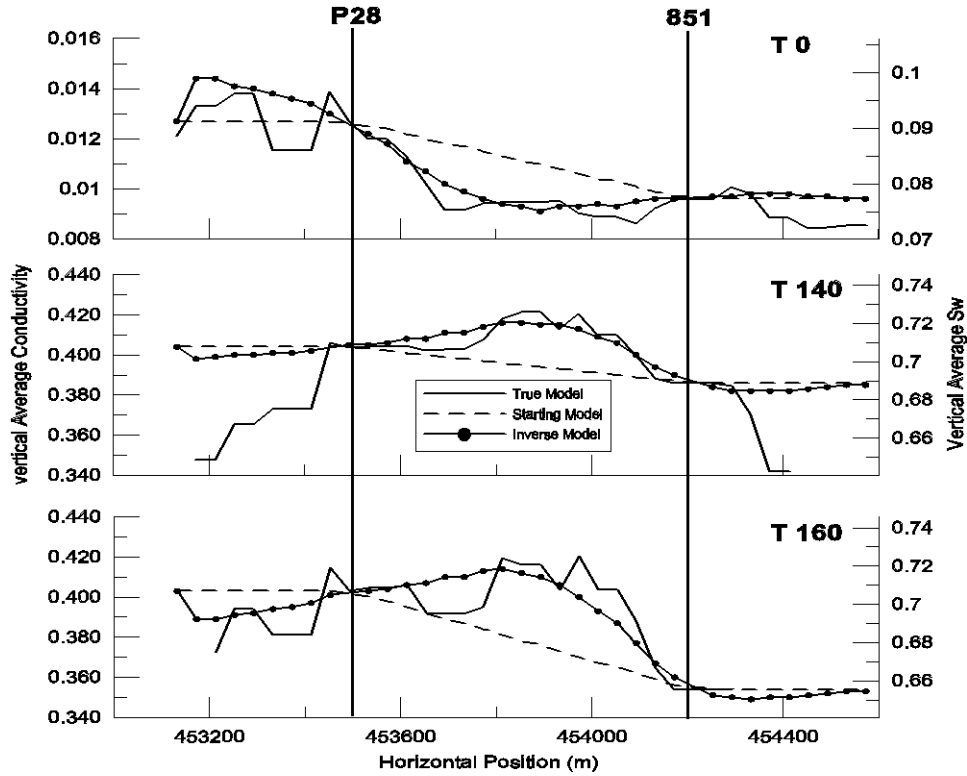


**Figure 10:** Comparison of vertically averaged conductivity and water saturation within the reservoir and that estimated from the cross-well inversions of numerical vertical and radial magnetic field data. Well P28 is located at distance 453474 m; well 851 is located at distance 454200m. Initial conditions are shown in the top panel. The middle panel shows reservoir at  $t_{140}$ . The bottom panel shows the reservoir at  $t_{160}$ .

As stated above the inversion using only the vertical magnetic field was unable to improve on the starting model in the  $t_0$  case. However, when the reservoir is resistive, at  $t_0$ , the radial magnetic field has a better signal to noise ratio (since noise is assumed to be a percentage of the total field) than the vertical field. To demonstrate the improvement in model resolution, inversions for the three time steps were run using both the radial and vertical magnetic fields. The resulting vertical average conductivity profiles are shown in Figure 10. The only important difference in the models comes at  $t_0$ , where the inversion is now able to reduce the conductivity in the interwell volume, more closely matching the true distribution. At the later times when the reservoirs average properties are closer to the background values (and the signal to noise ratio on the vertical component is largest) adding the radial field does not appreciably alter the final models.

Although lateral variations on the scale of a hundred meters, such as the low in conductivity and  $S_w$  between 463600 and 463800 at  $t_{160}$ , are not reproduced, the inversions do provide average properties between the wells which can not be deduced from the well sampling alone. In particular, the inversions show the reduction in conductivity and  $S_w$  between the wells at  $t_0$  and the increase in the same region at  $t_{140}$  and  $t_{160}$ . In addition the inversions predict the build up of oil near well 851 at  $t_{160}$  as seen by



the decrease in conductivity and  $S_w$  between 454100 and well 851 when the  $t_{140}$  and  $t_{160}$  predictions are compared.

## NOISE

As stated earlier we have in general assumed an optimistic Gaussian noise level with a standard deviation of 1% of the total magnetic field. In order to set some limits on what level of noise could be tolerated by the inversions at Snorre and still provide useful interwell conductivity and  $S_w$  estimates, we ran the inversions with various noise levels. Figure 11 shows the vertical average conductivity and  $S_w$  from three  $t_{140}$  models with one, two and three percent noise respectively. At four percent noise the inversion produced an anomalous low conductivity in the interwell region. The inversions with up to three percent noise show only small differences from one another but in general tended to reduce the estimate of the anomalous high conductivity in the interwell region as the noise increases. Inversions for  $t_{160}$  were very similar to  $t_{140}$  and the  $t_0$  inversions were able to tolerate five percent noise before losing the ability to predict the decrease in interwell conductivity. These tests indicate that for the Snorre example the maximum tolerable noise level is between 3 and 5 percent.

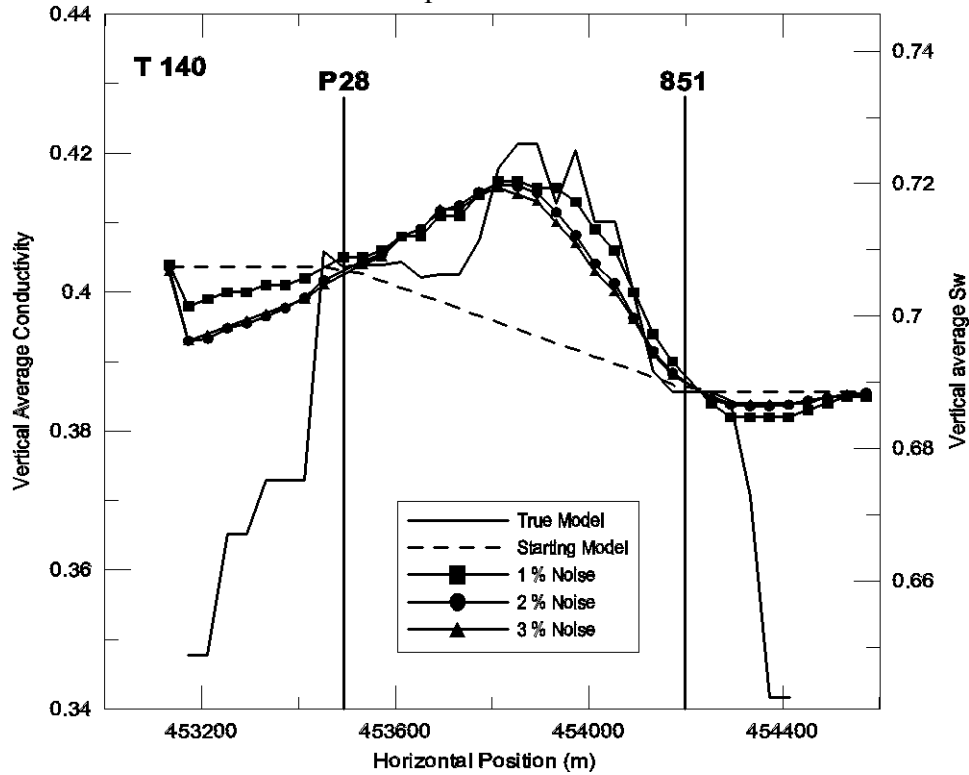


**Figure 11:** Effects of noise levels on  $t_{140}$  inversion of 2D data. As the noise level increases the estimated conductivity in the interwell region decreases. Beyond 3% random Gaussian noise the inversion does not predict the increase in interwell conductivity.

## THE EFFECTS OF CONSTRAINTS AND A PRIORI INFORMATION

The 2D inversions of 2D data previously discussed have all used both structural information from surface seismic to constrain the inversion domain to the reservoir and log conductivity data to provide a smooth reference model for inversion. It is important

to understand the contributions of structural constraints and a priori information on the spatial resolution of crosswell EM data. To this end we have generated four inversions of the  $t_{140}$  vertical magnetic field data with one percent noise. Figure 12 shows these inversions, the true conductivity section and fully constrained inversion are shown in panel b) of Figures 7 and 8 respectively. The vertical average conductivities within the reservoir for the four inversions along with the true model and fully constrained inversion are plotted in Figure 13.

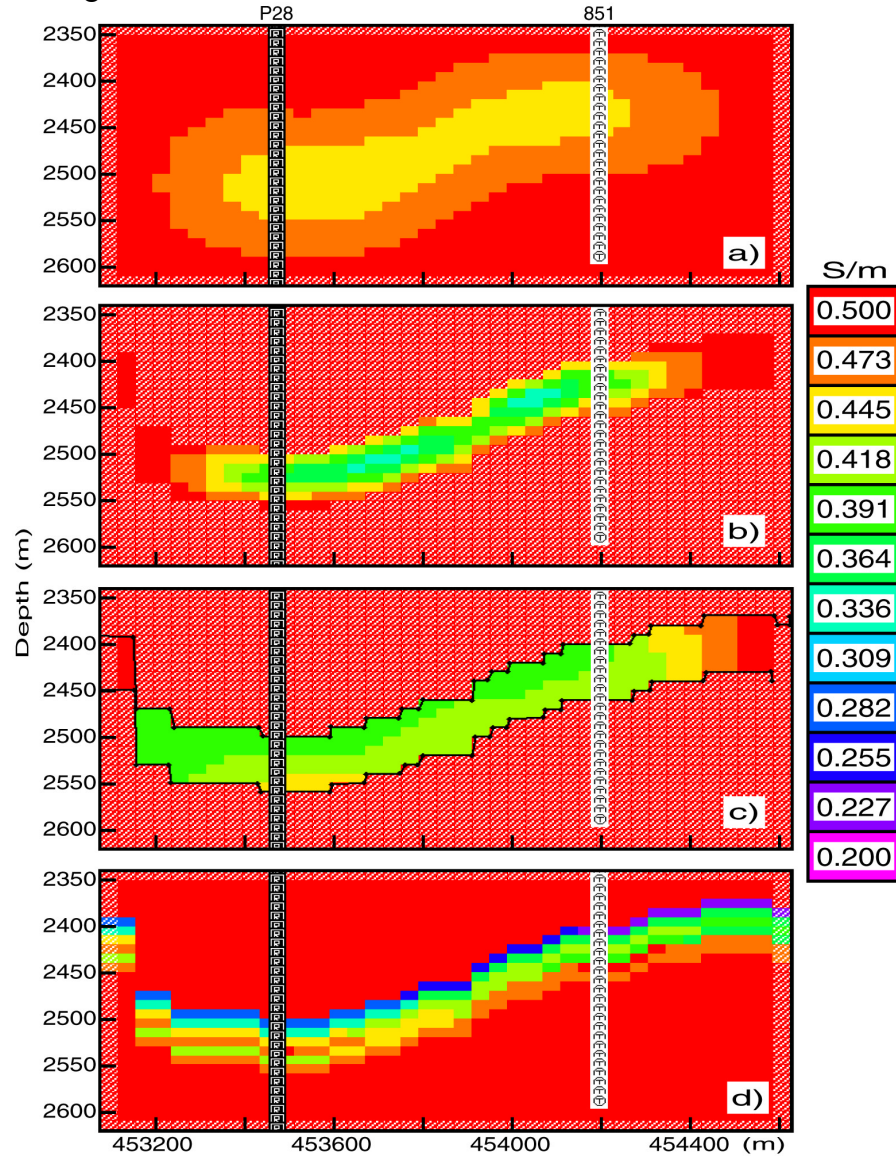


**Figure 12:** Four inversions of the 2D  $t_{140}$  vertical magnetic field data with 1% noise. Panel a) starting model was 0.5 S/m half space with no constraints. Panel b) starting model was 0.5 S/m half space but inversion domain was confined to the reservoir zone. Panel c) starting model was 0.5 S/m halfspace, inversion confined to reservoir zone and model smoothing stopped at reservoir boundaries. Panel d) starting model was linearly interpolated well log conductivities, no breaks in model smoothing and the entire cross section was free to change in the inversion.

Panel a) of Figure 12 shows the  $t_{140}$  inverse model when no structural constraints or a priori information is used. The starting model for the inversion was a half space of

0.5 S/m representing the surrounding shale. While the inverse model does show the correct reservoir geometry between the wells, the spatial smoothing (the regularization term  $(W(\sigma - \sigma_0))(W(\sigma - \sigma_0))^T$  in Equation (A6) of Appendix A) has spread the conductivity distribution over a much larger area than the reservoir, resulting in little detail within the reservoir zone itself. The vertical average conductivity shown in Figure 13 does show a qualitative indication of the increased conductivity in the interwell region but the entire curve is biased upward by its connection (through smoothing) to the 0.5 S/m material of the starting model outside of the inversion domain.

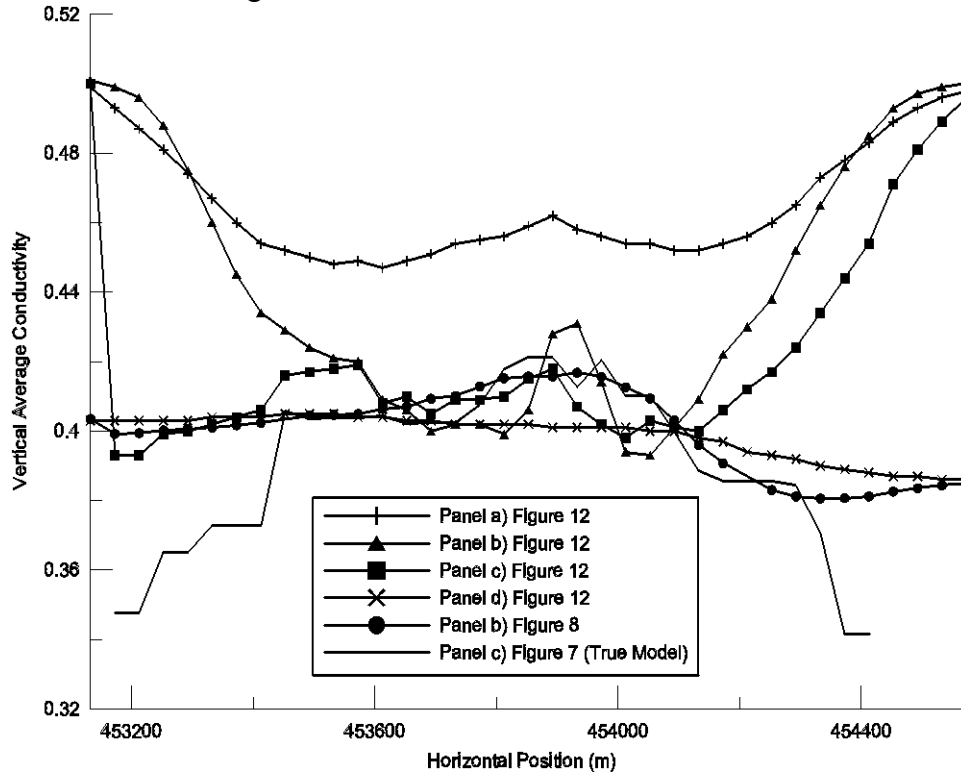


**Figure 13:** Vertical averaged conductivity from the four inverse models shown in Figure 12 and the fully constrained inverse shown in Figure 8 along with the true values from the model (panel b) in Figure 7.

Panel b) of Figure 12 shows the  $t_{140}$  inverse, again starting with a 0.5 S/m halfspace, where the inversion domain is limited to the reservoir only. In this case smoothing across the reservoir boundaries is still enforced causing a smooth gradation from the surrounding 0.5 S/m to the less conductive material in the center of the reservoir. The vertical average conductivity (Figure 13) again shows an indication of the increased conductivity in the interwell region but varies sharply laterally and swings up to the 0.5 S/m of the starting model on either end of the inversion domain.

Panel c) of Figure 12 shows the inverse model when the smoothing across the reservoir boundaries is eliminated. This allows the conductivity to jump across these boundaries. The starting model is still a 0.5 S/m halfspace. The impact of eliminating smoothing across boundaries in the model can be seen by comparing the conductivity estimates at the left end (453100) of the sections for panel b) and c). In the inversion shown in panel b) of Figure 12 the conductivity smoothly varies up to the edge value of 0.5 S/m. Whereas in the inversion of panel c) Figure 12, the break in smoothing which

coincides with the vertical fault in the reservoir at 453100m, allows the conductivity to remain low up to the fault. In this example the inversion not only indicates the increased conductivity in the interwell region but also shows an indication of the correct vertical variation in conductivity within the reservoir (less conductive at the top and more conductive at the bottom). This is significant because it indicates that there is sensitivity to vertical conductivity variations within the reservoir.

Finally, panel d) of Figure 12 shows the inverse where the starting model is the linearly interpolated well conductivities but where no constraints have been placed on the inversion domain and where the smoothing of the model perturbations exist across the reservoir boundaries. In this case very small changes have been made to the surrounding conductive material outside of the reservoir to accommodate the data. These changes (on the order of 5 to 10 %) do not show up on this color scale but are enough to fit the data while the vertical average conductivity within the reservoir changes little from the starting values.

These examples highlight the limitations of crosswell EM when used with no a priori information. It also demonstrates the significant improvement in spatial resolution of the vertically averaged reservoir conductivity (and thus the implied  $S_w$ ) that can be achieved when both structural information from seismic and a priori conductivity information from logs are incorporated. The case shown in Figure 12 panel c) with the vertical fault at 453100 also indicates the potential improvement in lateral resolution in the interwell region if seismic data could be used to provide the locations of faults.

## 2D INVERSION OF 3D DATA

The vertical magnetic field response from the 3D numerical model at  $t_{140}$  were inverted using the 2D algorithm previously described. Four well pairs were considered, (P28, 851), (P29, 851), (P25, 851) and (P18, 851). The 2D inversions all used starting and reference models constructed by linear interpolation of the well conductivities. Perturbations about the reference model within the reservoir zone were solved for with the smoothing eliminated across the reservoir boundaries. Figure 14 shows the vertical average conductivity for the four inverse models.

The section between P28 and 851 (Figure 2) is essentially perpendicular to the local structure. The 3D and 2D vertical magnetic fields differ by less than 5% at the extreme transmitter-receiver separations. As would be expected the 2D inverse of the 3D data predicts the interwell conductive as well as in the purely 2D case. At the other extreme is the section between P29 and 851, which is almost parallel to the local structure. This section, which should show the largest departure from a 2D response, is fairly well modeled by the 2D inversion. Figure 15 shows a comparison between 2D and 3D real and quadrature vertical magnetic fields for this section. The real components differ by a maximum of 3.5 percent when both the transmitter and receivers are within the reservoir. The quadrature component also differs by approximately 3.5 percent when

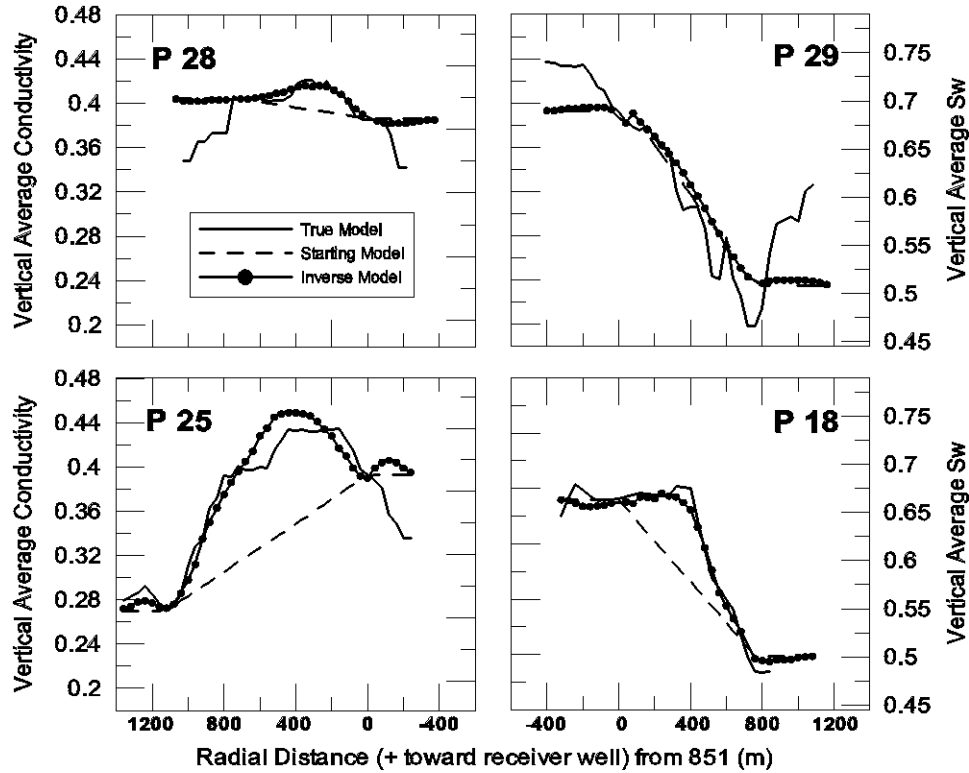


**Figure 14:** Vertical averaged conductivity and estimated Sw for the 4 crosswell sections shown in Figure 2. These were generated from 2D inversion of 3D vertical magnetic field data with 1% noise level. Upper left panel: section between 851 and P28. Upper right panel: section between 851 and P29. Lower left panel: section between 851 and P25, Lower right panel: section between 851 and P18.

the transmitter and receivers are within the reservoir. A maximum difference in the quadrature component of 40% occurs for the extreme transmitter-receiver separations. However these large differences occur at only a few data points in the quadrature component.

In order to understand the spatial distribution of model sensitivity we have computed the 3D Jacobian or, sensitivity matrix, for the 3D model at  $t_{140}$ . Rather than use the integral Equation solution for the sensitivity matrix from infinitesimal volumes in a whole space as done by Spies and Habashy (1995), we have used the ajoin method for the 3D finite difference solution, Newman and Alumbaugh (1997). The sensitivities were calculated for each cell in the 3D model (cell sizes 40x40x10 m) and normalized to the maximum value. Values of the normalized  $\log_{10}$  real vertical magnetic field sensitivity for a transmitter and receiver located within the reservoir at a depth of 2400m are contoured and overlaid on color contours of the vertical average reservoir conductivity in Figure 16. The -1 and -2 contours represent 1/10 and 1/100 of the maximum sensitivity respectively. Figure 16 shows that the sensitivity has dropped to 1/10 of the maximum for cells only 100 meters off line between the wells. In addition the distorting effects the variable conductivity distribution can be seen in the sensitivity pattern. In the interwell region the 0.5 contour encompasses a larger region farther away from well P29 compared to well 851 due to the decrease in conductivity near P29. All sensitivity contours are moved farther away from the wells in the less conductive areas compared to the more

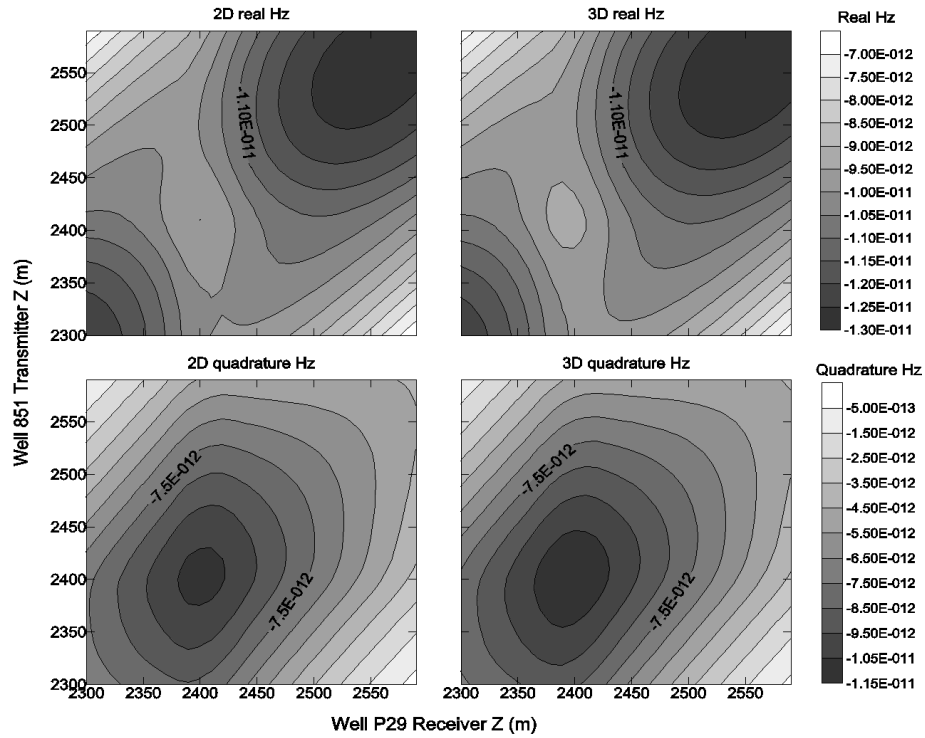


**Figure 15:** Comparison between 2D and 3D vertical magnetic fields calculated for transmitters in 851 and receivers in P29. This crosswell section is essentially parallel to local geologic strike.

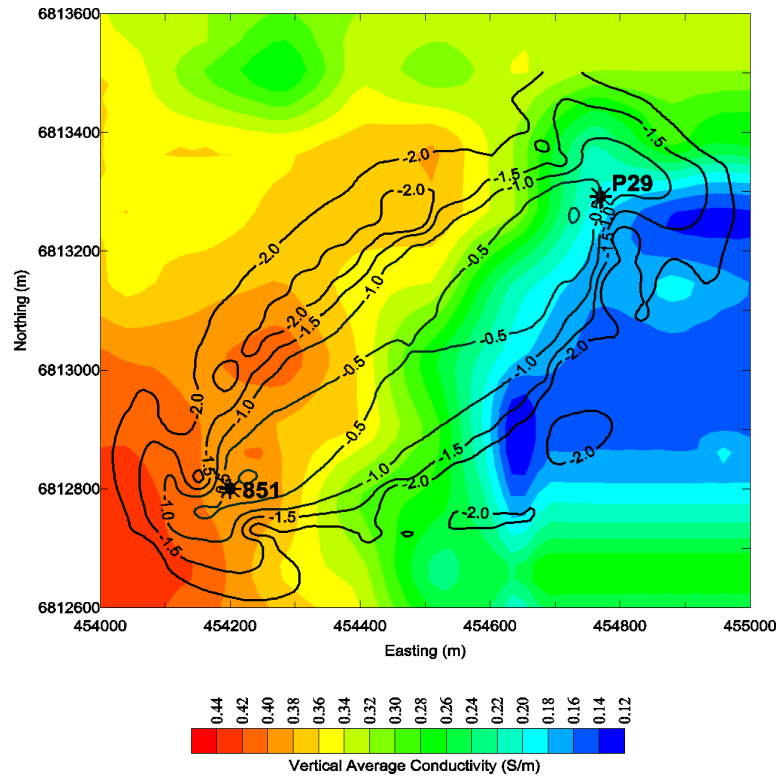


**Figure 16:** Vertical averaged conductivity within the reservoir at t140 shown in color contours. The 3D sensitivity (values of the Jacobian matrix) for a transmitter and receiver at a depth of 2400m (within the reservoir) are shown as black contour lines. The sensitivities are in  $\log_{10}$  of the normalized absolute value. Contour values of -1 and -2 represent 1/10 and 1/100 of the maximum sensitivity respectively.

conductive areas. Due to the asymmetry of the conductivity distribution cells 150 meters to the northwest in the more conductive material have only 1/100 the maximum sensitivity while to the southeast, in less conductive material, the 1/100 value is not reached until 200 meters off line.

The ability to reconstruct the vertical average reservoir conductivity between wells in this 3D geometry using 2D inversion is better than might be indicated by considering uniform whole space sensitivities. Spies and Habashy (1995) conclude that the strike length of a feature would have to be approximately equal to the source-receiver separation to appear 2D. While this statement is true it does not mean that 3D geology must meet this criteria for 2D inversion to be useful. In our example considerable conductivity variation occurs out of the plane of the transmitter and receiver wells within distances a fraction of the well separation. The ability to constrain the inversion domain to the reservoir zone and use a reference model generated from the log conductivity at the wells greatly improves the ability to predict the average reservoir conductivity between the wells. In general, at least for the Snorre example, 2D inversion of 3D data does a good job of representing the smoothed vertically averaged interwell reservoir conductivity.

## **CONCLUSIONS**

The forward modeling of the Snorre reservoir water flood has demonstrated two important facts that make the technique feasible for field use. First, a commercially available system would be able to produce measurable magnetic fields for the Snorre environment. Secondly, the observed vertical magnetic fields bear a strong qualitative relation to changes in the reservoir as water flood proceeds.

Two-dimensional inversions of crosswell EM data have the capability to provide quantitative predictions of the vertical average reservoir conductivity at different time steps of a petroleum reservoir water flood. In addition, provided relations between conductivity and  $S_w$  can be determined, they can also provide quantitative prediction of water saturation in the inter-well region. Two-dimensional inversions of fully 3D data for the Snorre example predict the vertically averaged reservoir conductivity almost as accurately as in the purely 2D example. This demonstrates that 2D inversion of crosswell EM data can provide useful information in realistic 3D petroleum reservoirs.

The ability to constrain crosswell EM inversions by incorporating reservoir structure from surface seismic data as well as provide reference models based on interpolated log conductivity greatly improves the ability to quantitatively map average reservoir conductivity. Without these constraints crosswell EM can map gross structural features and provide qualitative estimates of relative high and low conductivity zones in the interwell region but cannot predict conductivity accurately enough to be used in estimates of water saturation.

## **DISCUSSION**

This study is a beginning. Crosswell EM is a technique with the ability to map conductivity, and hence infer water saturation, in the interwell volume on a scale that can

provide useful updates to reservoir simulations. The maximum benefit from the technique will be derived when it is used in conjunction with both seismic data and production history matching by reservoir simulation. In the example presented here seismic data was essential to provide the reservoir geometry. This greatly constrains the volume available for the EM inversion to update and thus greatly reduces problems of non-uniqueness. Additional data sets will provide more detailed starting models (reference models) for the EM inversions. We see the process as an iterative one in which the models (reservoir simulation, seismic velocity and electrical conductivity) feed back to one another until all data is satisfied with a self-consistent rock-properties model. That is, the porosity, water saturation, velocity, and resistivity can all be explained by one set of empirical relations that match observed well log and laboratory data. In this example where no interwell information was built into the reference model the linear interpolation of log values provided a smooth reference model. When additional information from either reservoir simulation models or seismic is used to provide reference models with more internal structure, crosswell EM inversion can be used to solve for perturbations about these more detailed models which satisfy the EM data.

A significant benefit will be derived when either crosswell seismic and/or surface seismic is used to provide estimates of the interwell porosity. In many situations the pore fluid will be considerably more conductive than the injected water. In these cases the porosity will become an additional parameter since an accurate bulk resistivity estimate will require mixing of the two different fluid resistivities within the pore space.

We intend to continue working on this and other examples by extending the inversion work to 3D. Working in 3D increases the computational load significantly but is still possible on current high-end workstations. For larger scale 3D inversion applications, massively parallel computing platforms can be utilized (cf. Newman and Alumbaugh, 1997).

### **ACKNOWLEDGEMENTS**

The authors are grateful to Mike Wilt for his many useful comments and information on the state of the art in crosswell EM systems. We also thank Saga Petroleum ASA for permission to publish this work. This work was funded in part by the Assistant Secretary for Fossil Energy, National Petroleum Office of the U.S. Department of Energy under Contract No. DE-AC03-76SF00098 and Sandia Contract # DE-AC04-94AL85000.

### **REFERENCES**

- Alumbaugh, D. L., Becker, A., Morrison, H. F., Lee, K. H., Wilt, M. J., 1993, Saltwater injection monitoring with cross-hole EM; a report of 1992 field activities at the UC Richmond Field Station: Lawrence Berkeley National Laboratory Report LBL-33000.
- Alumbaugh D. L. and Morrison, H. F., 1993, Electromagnetic conductivity imaging with an iterative Born inversion: IEEE Trans. Geosci. Remote Sensing, **31**, 758-763.



Alumbaugh D. L. and Morrison, H. F., 1995, Theoretical and practical considerations for crosswell electromagnetic tomography assuming a cylindrical geometry: *Geophysics*, **60**, 846-870.

Archie, G. E., 1942, The electrical resistivity log as an aid in determining some reservoir characteristics: *Trans. AIME*, **146**, 54-61.

Becker, A., Wang, B., Lee, K.H. and Wilt, M., 1998, Subsurface Electromagnetic Measurement through Steel Casing: Lawrence Berkeley National Laboratory Report LBNL-42375.

Diesen, G.W., Edvardsen, A., Nystuen, J.P. and Tollefsrud, J.I., 1995, Geophysical and geological tools and methods used for reservoir characterization and modelling of the Snorre Field - North Sea, Norway: Special Publication of the Technology Research Centre, JNOC, **5**, 69-90.

Fletcher, R., and Jackson, M. P., 1974, Minimization of a quadratic function of many variables subject only to lower and upper bounds: *J. Inst. Math. Applics.*, **14**, 159-174.

Lake, L.W., 1990, What engineers need for numerical simulation: Univ. of Arizona and SEG Internat. Symposium on Borehole Geophysics: Petroleum, Hydrogeology, Mining and Engineering Applications, Feb. 1990.

Lee, K. H. and Kim, H. J., 1998, Electromagnetic Method for Analyzing the Property of Steel Casing: Lawrence Berkeley National Laboratory Report LBNL-41525.

Newman, G., A., and Alumbaugh, D. L., 1997, Three-dimensional massively parallel electromagnetic inversion – I .Theory: *Geophys. J. Int.*, **128**, 345-354.

Newman, G. A., 1995, Crosswell electromagnetic inversion using integral and differential Equations: *Geophysics*, **60**, 899-911.

Savit, C., 1987, New ways to study the earth, in: Research needs for hydrocarbon fuels, Workshop report on: not yet visible or recoverable hydrocarbons, May 11-13, Houston Area Research Center, U.S. D.O.E., Office of Basic Energy Science, CONF-8705179, 16-18.

Shelton, J.L. and Cross, T.A., 1989, The influence of stratigraphy in reservoir simulation, *Quantitative Dynamic Stratigraphy*, 589-600. Prentice-Hall.

Song, Y. and Lee, Ki Ha, 1998, Electromagnetic Fields Due to a Loop Current in a Cased Borehole Surrounded by Uniform Whole Space: Lawrence Berkeley National Laboratory Report LBNL-42371.

Spies, B. R., 1992, Survey design for cross-well electromagnetics: 62nd Ann. Internat. Mtg., Soc. Expl. Geophys., Expanded Abstracts, 498-501.

Spies, B. R., And Habashy, T. M., 1995, Sensitivity analysis of cross-well electromagnetics: *Geophysics*, **60**, 834-845.

Suman, R. J. and Knight, R. J., 1997, Effects of pore structure and wettability on the electrical resistivity of partially saturated rocks - A network study: *Geophysics*, **62**, 1151-1162.

Tikhonov, A. N., and Arsenin, V. Y., 1977, *Solutions to ill-posed problems*: John Wiley and Sons, Inc.

Wang, T., Hohmann, G. W., 1993, A finite difference time-domain solution for three-dimensional electromagnetic modeling: *Geophysics*, **58**, 797-809.

Wilt, M. J., Alumbaugh, D. L., Morrison, H. F., Becker, A., Lee, K. H., and Dezc-Pan, M., 1995, Crosshole electromagnetic tomography: design considerations and field results: *Geophysics*, **60**, 871-885.

Wilt, M. J., Morrison, H. F., Becker, A., Tseng, H. W., Lee, K. H., Torres-Verdin, C., and Alumbaugh, D. L., 1995, Crosshole electromagnetic tomography: a new technology for oil field characterization: *The Leading Edge*, **14**, 173-177.

Wu, X. and Habashy, T. M., 1994, Influence of steel casings on electromagnetic signals: *Geophysics*, **59**, 378-390.

Zhou, Q., 1989, *Audio-frequency electromagnetic tomography for reservoir evaluation*: Lawrence Berkeley Laboratory Report LBL-28171.

Zhou, Q., Becker, A., Morrison, H. F., 1993, Audio-frequency electromagnetic tomography in 2-D: *Geophysics*, **58**, 482-495.

## APPENDIX A - Inverse Modeling

Given a 3-D conductivity distribution in the earth,  $\sigma(\mathbf{r})$ , the EM fields, neglecting displacement currents, can be described by the integral equation

$$\mathbf{d}^{\mathbf{F}_p}(\mathbf{r}) = \mathbf{d}^{\mathbf{F}^{(i)}}(\mathbf{r}) + \int_V \mathbf{G}^{\mathbf{F}^{(i)}}(\mathbf{r}, \mathbf{r}') \mathbf{E}(\mathbf{r}') (\sigma(\mathbf{r}) - \sigma^{(i)}(\mathbf{r})) d\mathbf{v}' \quad (\text{A1})$$

where  $\mathbf{d}^{\mathbf{F}_p}$  is the computed electric or magnetic field.  $\mathbf{d}^{\mathbf{F}^{(i)}}$  is the background electric or magnetic field and  $\mathbf{G}^{\mathbf{F}^{(i)}}(\mathbf{r}, \mathbf{r}')$  is the electric or magnetic field tensor Green's function. Since  $\mathbf{E}$  is also a function of  $\sigma(\mathbf{r})$ , Equation (A1) is non-linear in  $\sigma$ . The superscript (i) refers to some background model, and  $\mathbf{E}(\mathbf{r}')$  is the internal electric field. This background model, its fields, and the Green's functions are not required to be one-dimensional and are assumed to be known. The internal electric field,  $\mathbf{E}(\mathbf{r}')$ , is however unknown.

Equation (A1) can be written in discrete form, specialized for two dimensional crosswell configurations. The integration over the volume is replaced by two summations over  $N_{xz}$  cells in the crosswell (x-z) plane and  $N_y$  cells along the y axis or strike direction. Specifically,

$$\mathbf{d}^{\mathbf{F}_p}(\mathbf{r}_k) = \mathbf{d}^{\mathbf{F}^{(i)}}(\mathbf{r}_k) + \sum_1^{N_{xz}} (\sigma(\mathbf{r}_n) - \sigma^{(i)}(\mathbf{r}_n)) \bullet \sum_1^{N_y} \tilde{\Gamma}^{\mathbf{F}^{(i)}}(\mathbf{r}_k, \mathbf{r}_{n,j}) \mathbf{E}(\mathbf{r}_{n,j}) \quad (\text{A2})$$

where the tensor Green's function for a prism of current with its center at  $\mathbf{r}_{n,j}$  is defined as

$$\tilde{\Gamma}^{\mathbf{F}^{(i)}}(\mathbf{r}_k, \mathbf{r}_{n,j}) = \int_{\tilde{v}_{nj}} \mathbf{G}^{\mathbf{F}^{(i)}}(\mathbf{r}_k, \mathbf{r}') d\mathbf{v}' \quad (\text{A3})$$

Because the conductivity in Equation (A2) does not depend on the index  $j$ , but only on  $n$ , it is a 2-D distribution.

The major difficulty in using (A2) to obtain estimates of  $\sigma(\mathbf{r}_n)$  is that it is nonlinear in  $\sigma(\mathbf{r}_n)$ . Equation (A2) can be linearized using the Born approximation, where the electric field is that of the background. Thus under the Born approximation, (A2) is written as

$$\mathbf{d}^{\mathbf{F}_p}(\mathbf{r}_k) = \mathbf{d}^{\mathbf{F}^{(i)}}(\mathbf{r}_k) + \sum_1^{N_{xz}} \tilde{\mathbf{A}}_{k,n}^{\mathbf{F}^{(i)}} (\sigma(\mathbf{r}_n) - \sigma^{(i)}(\mathbf{r}_n)) \quad (\text{A4})$$

where

$$\tilde{\mathbf{A}}_{k,n}^{\mathbf{F}^{(i)}} = \sum_{j=1}^{N_y} \tilde{\Gamma}^{\mathbf{F}^{(i)}}(\mathbf{r}_k, \mathbf{r}_{n,j}) \mathbf{E}^{(i)}(\mathbf{r}_{n,j}). \quad (\text{A5})$$

### Regularized least squares

Because the inverse problem is underdetermined, it is unstable and ill posed. Reliable estimates of  $\sigma(\mathbf{r}_n)$  may be possible if (A4) is stabilized in a least-squares sense

with regularization (Tikhonov and Arsenin, 1977). Regularization removes solutions that are too rough by adding a model roughness term to the object function being minimized. Reconstructions are required to be smoothed versions of the earth's electrical properties at the expense of an increase in the fitting error.

The following functional can provide smooth reconstructions if it is minimized with respect to the model parameters  $\sigma(\mathbf{r}_n)$  subject to inequality constraints:

$$S = \lambda^{-1} \left[ (\mathbf{D}(\mathbf{d}^F - \mathbf{d}^{F(i)} - \mathbf{A}^{F(i)}(\sigma - \sigma^{(i)})))^T (\mathbf{D}(\mathbf{d}^F - \mathbf{d}^{F(i)} - \mathbf{A}^{F(i)}(\sigma - \sigma^{(i)}))) - \chi^2 \right] + \beta (\mathbf{W}(\sigma - \sigma_0))^T (\mathbf{W}(\sigma - \sigma_0)) \quad (\text{A6})$$

Here we minimize model roughness  $(\mathbf{W}(\sigma - \sigma_0))^T (\mathbf{W}(\sigma - \sigma_0))$  subject to a specified squared error  $\chi^2$ . The superscript T denotes the transpose operator. The matrix W is the roughness matrix consisting of a finite difference approximation to the Laplacian ( $\nabla^2$ ) operator. In (A6) the vector  $\mathbf{d}^F$  is the observed data. The data weighting matrix D can take many forms, however in our case it is diagonal and contains the reciprocal of the data standard deviations. The last term in (A6) is added in order to solve for perturbations about some reference model  $\sigma_0$ .

The parameter  $\lambda$  is the tradeoff parameter between model smoothness and data fit. Its selection requires special care if the inverse solution is to provide acceptable results. There is no universal or unique strategy for selecting  $\lambda$  in (A6). It is important, however, to select it such that there is an acceptable tradeoff between model smoothness and the data fit. Selecting tradeoff parameters that are too small can produce models that are physically unreasonable in that the models are spatially too rough but can produce superior data fits. Selecting tradeoff parameters that are too large produce highly smoothed models, but these models show poor dependence of the data.

Because (A6) is a quadratic functional, its minimization subject to inequality constraints is a linear programming problem. Solution to this problem can be found using the algorithm of Fletcher and Jackson (1974). Inequality constraints are incorporated into the inverse problem to omit solutions that are not reasonable given prior information.

The inversion algorithm was modified to accommodate fixing of cell resistivities outside the reservoir and placing tears in the smoothing matrix. This enabled us to only invert for a smooth conductivity distribution within the reservoir zone. The boundaries of the reservoir were defined by surface 3D seismic data. These boundaries were used to place tears in the smoothing so that the inverse model did not smooth resistivities across the top and base of the reservoir.